

Multi-objective-global-optimization-approach predicted quasi-layered ternary TiOS crystals with promising photocatalytic properties

Yi-Jie Xiang(向依婕), Siyan Gao(高思妍), Chunlei Wang(王春雷), Haiping Fang(方海平), Xiangmei Duan(段香梅), Yi-Feng Zheng(郑益峰), and Yue-Yu Zhang(张越宇)
Citation: Chin. Phys. B, 2024, 33 (**8**): 087101. DOI: 10.1088/1674-1056/ad4bc3

What follows is a list of articles you may be interested in

Blue phosphorene/$MoSi_2N_4$ van der Waals type-II heterostructure: Highly efficient bifunctional materials for photocatalytics and photovoltaics

Xiaohua Li(李晓华), Baoji Wang(王宝基), and Sanhuang Ke(柯三黄)
Chin. Phys. B, 2023, 32 (**2**): 027104. DOI: 10.1088/1674-1056/ac9469

Interfacial defect engineering and photocatalysis properties of hBN/MX_2 (M = Mo, W, and X = S, Se heterostructures

Zhi-Hai Sun(孙志海), Jia-Xi Liu(刘佳溪), Ying Zhang(张颖), Zi-Yuan Li(李子源), Le-Yu Peng(彭乐宇), Peng-Ru Huang(黄鹏儒), Yong-Jin Zou(邹勇进), Fen Xu(徐芬), and Li-Xian Sun(孙立贤)
Chin. Phys. B, 2022, 31 (**6**): 067101. DOI: 10.1088/1674-1056/ac43b2

Interfacial properties of g-C_3N_4/TiO_2 heterostructures studied by DFT calculations

Chen-Shan Peng(彭春山), Yong-Dong Zhou(周永东), Sui-Shuan Zhang(张虽栓), and Zong-Yan Zhao(赵宗彦)
Chin. Phys. B, 2021, 30 (**1**): 017101. DOI: 10.1088/1674-1056/abb30b

Electronic structures of efficient $M$$BiO_3$ (M = Li, Na, K, Ag) photocatalyst

Wen-Liu Zhou(周文流), Zong-Yan Zhao(赵宗彦)
Chin. Phys. B, 2016, 25 (**3**): 037102. DOI: 10.1088/1674-1056/25/3/037102

Growth of monodisperse nanospheres of $MnFe_2O_4$ with enhanced magnetic and optical properties

M. Yasir Rafique, Pan Li-Qing (潘礼庆), Qurat-ul-ain Javed, M. Zubair Iqbal, Qiu Hong-Mei (邱红梅), M. Hassan Farooq, Guo Zhen-Gang (郭振刚), M. Tanveer
Chin. Phys. B, 2013, 22 (**10**): 107101. DOI: 10.1088/1674-1056/22/10/107101

Multi-objective global optimization approach predicted quasi-layered ternary TiOS crystals with promising photocatalytic properties

Yi-Jie Xiang(向依婕)[1,2], Siyan Gao(高思妍)[3], Chunlei Wang(王春雷)[1,4], Haiping Fang(方海平)[5], Xiangmei Duan(段香梅)[6], Yi-Feng Zheng(郑益峰)[2,7,†], and Yue-Yu Zhang(张越宇)[2,7,‡]

[1] *Shanghai Institute of Applied Physics, Chinese Academy of Sciences, Shanghai* 201800, *China*
[2] *University of Chinese Academy of Sciences, Beijing* 100049, *China*
[3] *School of Materials Science and Engineering, East China University of Science and Technology, Shanghai* 200237, *China*
[4] *College of Science, Shanghai University, Shanghai* 200444, *China*
[5] *School of Physics, East China University of Science and Technology, Shanghai* 200237, *China*
[6] *School of Physical Science and Technology, Ningbo University, Ningbo* 315211, *China*
[7] *Wenzhou Institute, University of Chinese Academy of Sciences (UCAS), Wenzhou* 325001, *China*

(Received 11 May 2024; revised manuscript received 12 May 2024; accepted manuscript online 15 May 2024)

Titanium dioxide (TiO_2) has attracted considerable research attentions for its promising applications in solar cells and photocatalytic devices. However, the intrinsic challenge lies in the relatively low energy conversion efficiency of TiO_2, primarily attributed to the substantial band gaps (exceeding 3.0 eV) associated with its rutile and anatase phases. Leveraging multi-objective global optimization, we have identified two quasi-layered ternary Ti–O–S crystals, composed of titanium, oxygen, and sulfur. The calculations of formation energy, phonon dispersions, and thermal stability confirm the chemical, dynamical and thermal stability of these newly discovered phases. Employing the state-of-art hybrid density functional approach and many-body perturbation theory (quasiparticle GW approach and Bethe–Salpeter equation), we calculate the optical properties of both the TiOS phases. Significantly, both phases show favorable photocatalytic characteristics, featuring band gaps suitable for visible optical absorption and appropriate band alignments with water for effective charge carrier separation. Therefore, ternary compound TiOS holds the potential for achieving high-efficiency photochemical conversion, showing our multi-objective global optimization provides a new approach for novel environmental and energy materials design with multicomponent compounds.

Keywords: photocatalysis, first principles calculations, multi-objective global optimization

PACS: 71.15.Mb, 71.20.–b, 71.20.Nr, 71.35.Cc **DOI:** 10.1088/1674-1056/ad4bc3

1. Introduction

With the increasingly serious worldwide climate disruption, there is an urgent need to search for renewable energy alternatives, such as new high-efficiency solar absorbers and photochemical materials that can effectively utilize solar energy. Titanium dioxide (TiO_2) is a robust, thermally stable, and inexpensive material with abundant physical and chemical properties, which makes it competitive in many applications fields,[1–4] such as medicine,[5] optoelectronic devices,[6] and so on, especially in the field of photocatalysis. It was first discovered as a photocatalyst for hydrogen evolution in 1972.[7,8] As one of the core materials in the field of photocatalysis, polycrystalline TiO_2 (rutile, anatase, and brookite) have become the most widely studied photocatalyst among metal oxides,[9] and its application potential in promoting sustainable energy technology and environmental protection is enormous.[10–16] However, the significant disadvantages of TiO_2 as a photocatalyst lie in its narrow visible optical absorption range and high photo-generated electron recombination rate due to its large band gap,[17,18] which makes it challenging to achieve high efficiency for photocatalysis.

To improve the solar energy absorption of TiO_2 in the visible light range, various modification methods have been employed and doping is one of the most effective ways.[19–23] Doping impurity elements will introduce impurity energy levels within the band gap of TiO_2, thereby exhibiting visible light-responsive photocatalytic reactivity and showing greater stability upon UV irradiation.[24] There are two ways of doping based on the type of doped element, metal doping and nonmetal doping. For metal doping, it exhibits several drawbacks, such as the thermal instability of TiO_2, high modification cost, and the introduction of electron/hole recombination centers.[24] To overcome these challenges, metal self-doping[25] and non-metal doping are applied. These technics includes Ti^{3+} self-doping, and anion doping such as introducing N,[26] S,[27] and C[28] into TiO_2.[29]

Among all the doping methods, S doping is particularly promising because (i) S atoms have the same valence as O

†Corresponding author. E-mail: zhengyifeng@ucas.ac.cn
‡Corresponding author. E-mail: zhangyy@wiucas.ac.cn

© 2024 Chinese Physical Society and IOP Publishing Ltd

atoms and can occupy at the O sites;[30] (ii) S 3p orbital is energetically higher than O 2p orbital; (iii) S doping adjusts the position of the valence band maximum (VBM) without changing the conduction band minimum (CBM), while the CBM of TiO_2 is near the threshold of the energy for hydrogen formation. Experimentally, as early as 2002, Umebayashi *et al.* had synthesized S-doped TiO_2 by oxidation annealing of TiS_2 and observed a significant shift of the absorption edge towards the low-energy region.[31] In subsequent experimental studies, other S precursors[32–36] and various different doping methods[33,34,37–40] were used to achieve higher doping efficiency and concentration of S, which further enhance visible optical absorption and photocatalytic properties.

Theoretical studies on sulfur doping in TiO_2 focus more on the electronic structure change induced by O substituted by S than the structural change induced by high-concentration of S doping. Electronic structure analysis reported by Cui *et al.*[41] showed that the narrowing of the band gap can be attributed to the isolated S 3p state appearing on the upper edge of the valence band of S-doped TiO_2. The relevant research also considered the different oxidation states of sulfur in TiO_2 and found that different doping configurations have different effects on electronic structure and optical absorption characteristics, which optimizes the photocatalytic efficiency of TiO_2.[42,43] Recently, Jovanović *et al.*[44] studied $TiO_{1-x}S_x$ ($x = 0$, 0.25, 0.5, 0.75, and 1) crystal structures adopting anatase, rutile, and CdI_2 structure types, and found very interesting pressure-induced phase transitions in the TiOS compounds. However, doping, especially in a very high concentration, could possibly alter the crystal structure and atomic transmutation while keeping the parent lattice unchanged may not be enough. For example, when S is doped into the TiO_2 lattice in anionic (S^{2-}) form and substitutes for oxygen atoms in the rutile unit cell, it not only introduces S-derived energy levels in the band gap of TiO_2, but also causes Ti atoms to move out of the plane, disrupting the lattice symmetry of rutile.[45] Therefore, more advanced methods beyond the conventional atomic transmutation should be considered to explore the global energy minima and optical properties of structures.

Motivated by above considerations, in this work, we use a multi-objective global optimization algorithm combined with first principles calculations to search for new TiOS configurations with both low energy and suitable visible optical absorption band gap for oxygen and sulfur ratios of 50% each. Two new phases that are named after their space group as TiOS_$P2_1/m$ and TiOS_$P3m1$ are predicted to be chemically, dynamically, and thermally stable. The electronic structures of both phases are evaluated by state-of-art HSE06 functional and GW/BSE method,[46,47] which accurately predict that both phases have sufficient optical absorption efficiency in the visible light range and can also be used as good photocatalysts for water decomposition in a wide pH range. Furthermore, the multi-objective global optimization is universal, it holds the potential to design more functional compounds with different compositions.

2. Computational methods

2.1. Crystal structures predicted by multi-objective differential evolution

In this work, we perform a multi-dimensional global optimization algorithm, as implemented in the IM^{2}ODE package developed by our group,[48,49] to search for TiOS with the band gap suitable for solar absorption. After local optimization of atomic coordinates and lattice constants, the electronic band structure can be calculated to obtain the band gap E_g. In order to find TiOS with a low formation energy and a suitable band gap E_g^{opt} for optical absorption, we define the fitness functions as

$$\min z_1 = \text{total energy}, \tag{1}$$

$$\min z_2 = \left|E_g^{opt} - E_g\right|. \tag{2}$$

The transition matrix element between the VBM and CBM is also included in the designing process so that if the transition at the direct band gap is forbidden, z_2 is set to be infinite to exclude optically inactive structure. Then, the multi-objective differential evolution (MODE) algorithm is performed to select and generate new structures. The number of atoms of the unit cell is enumerated from 3 to 24. In the structure searching progress, the population size is 30 and the number of generations is 20. The size/shape of the unit cell is updated with the lowest energy each generation. The objective band gap E_g^{opt} is set to 0.8 eV in the PBE calculation as it underestimates the band gap.

2.2. Density functional theory calculations

We perform the structural relaxations and the electronic structure calculations based on density functional theory (DFT). The ion–electron interaction is treated by projector augmented wave (PAW) method,[50] as implemented in the Vienna *Ab initio* Simulation Package (VASP) code.[51–54] The exchange–correlation interaction between electrons is treated by the Perdew–Burke–Ernzerhof (PBE) functional[54] of generalized gradient approximation (GGA).[55] The plane wave cutoff of 600 eV is used, and the structural relaxation is performed until the total energy and Hellmann–Feynman force are below 10^{-6} eV and 10^{-1} eV/Å, respectively. The k-mesh based on Monkhorst–Pack scheme[56] is $12 \times 7 \times 6$ for TiOS_$P2_1/m$ and $13 \times 6 \times 6$ for TiOS_$P3m1$, respectively. Then, the band gap and optical properties are re-computed by employing the HSE06[57] functional, which is found to give more accurate band gaps than PBE for semiconductors. We

use the frozen phonon method as implemented in PHONOPY code[58] to check the dynamic stability of the specific structures. *Ab initio* molecular dynamics (AIMD) simulations are executed by using the NVT canonical ensemble with the Nosé Hoover thermostat at 300 K using VASP code. The sizes of supercells used in simulations are 19.34 Å × 19.21 Å × 18.91 Å and 19.07 Å × 19.07 Å × 17.74Å for TiOS_$P2_1/m$ and TiOS_$P3m1$, respectively. A single Gamma point is used to sample the Brillouin zone. Each AIMD simulation runs for 15 ps with a time step of 3.0 fs.

2.3. G_0W_0–BSE calculations

For excited states, the results obtained from DFT calculations are usually not very accurate, so GW and BSE methods are widely used. In this study, quasiparticle (QP) energy calculations with the single shot G_0W_0 approximation[59] and neutral excitation spectra by solving the Bethe–Salpeter equation (BSE)[60] are both carried out with VASP.[51–54] First, the self-consistent DFT eigenvalues and Kohn–Sham orbitals are obtained based on calculations of PBE functional. Subsequently, the DFT Green's function G_0 and the dynamically screened interaction W_0 are constructed. RPA quasiparticles are calculated using the single-shot GW method. The electron–hole interaction is included in the BSE. The coupling term is ignored to simplify the calculation, which is referred to as the Tamm–Dancoff approximation (TDA). Four valance band states and eight conduction band states are included in the basis for diagonalization of the BSE Hamiltonian. Calculations are carried out using the primitive cell. The energy cutoff for response function is 150 eV. The number of frequency bands used in G_0W_0 calculation is 128.

3. Results and discussion

3.1. Structure and stability of the TiOS

We search for possible TiOS compounds under ambient conditions and find two stable ternary compounds satisfying the following criteria: (i) the formation energy with respect to elemental Ti, O, and S is negative; (ii) the band gap calculated by HSE06 is in the range of 1.0 eV–1.5 eV; (iii) the structure is dynamically stable without imaginary phonon mode. The two metastable phases are named after their space group as TiOS_$P2_1/m$ and TiOS_$P3m1$, which are represented by green solid dots in the Ti–O–S phase diagram (Fig. 1(a)). The TiOS_$P3m1$ phase was first reported by Jovanović *et al.*[44] through atomic transmutation of the CdI_2 phase of TiS_2 while TiOS_$P2_1/m$ is energetically more favorable.

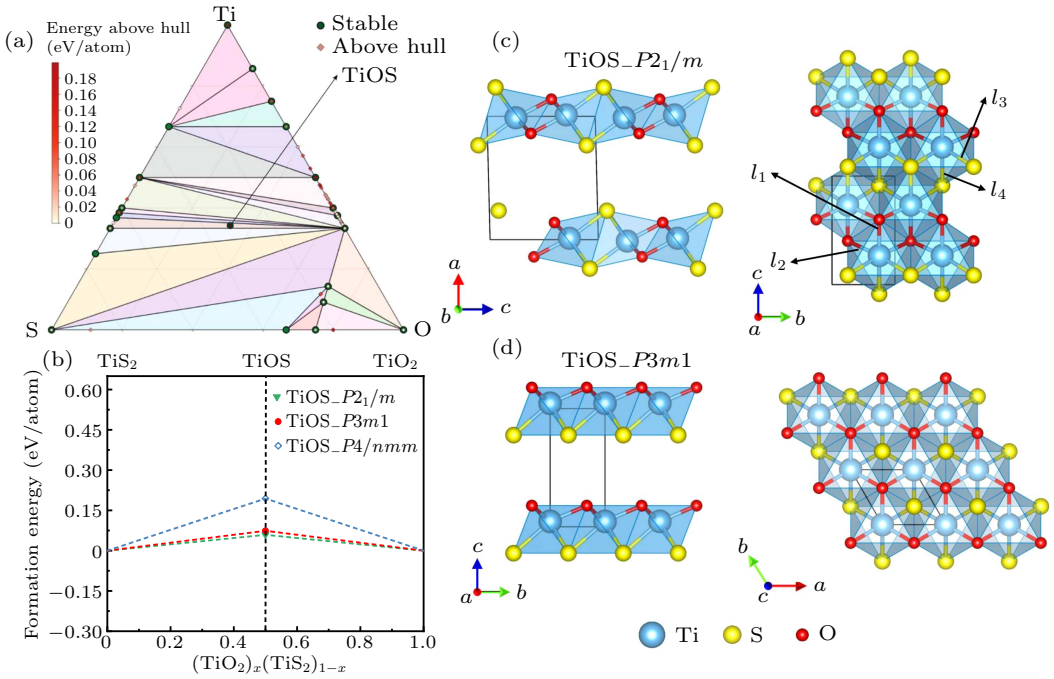


Fig. 1. The energies and crystal structures of the predicted Ti–O–S compounds under ambient conditions. (a) Ti–O–S ternary phase diagram. Green circles represent the stable phases and the diamond shaped dots represent unstable structure whose colors represent values of energies higher than the ground state. (b) The energies for TiOS_$P2_1/m$, TiOS_$P3m1$ (atomic transmutation of CdI_2 phase reported in Ref. [44]) and TiOS_$P4/nmm$ (atomic transmutation of rutile phase reported in Ref. [61]). The crystal structures of (c) TiOS_$P2_1/m$, (d) TiOS_$P3m1$. Ti, O, and S atoms are represented by blue, red, and yellow spheres, respectively.

The formation energy with respect to elementary substances Ti, O, S is

$$E_{\mathrm{f}}^{\mathrm{TiOS}} = \left(E\left(\left(\mathrm{TiOS}\right)_n\right) - n \times \left(E\left(\mathrm{Ti}\right) + E\left(\mathrm{O}\right) + E\left(\mathrm{S}\right)\right)\right)/N, \quad (3)$$

where $E\left(\left(\mathrm{TiOS}\right)_n\right)$ is the total energy of the TiOS unit cell, n is the number of formulas per unit cell of TiOS, E(Ti), E(O), E(S) are the energies of individual atoms Ti, O, S, respectively, and N is the number of atoms within the TiOS

unit cell. The calculated formation energy of TiOS_$P2_1/m$ is −2.043 eV/atom, while the formation energy of TiOS_$P3m1$ is −2.027 eV/atom, which is only 0.017 eV/atom higher than the formation energy of TiOS_$P2_1/m$. If we consider the case of TiOS degradation to TiO_2 and TiS_2, using the similar approach, we can also calculate the formation energy with respect to the ground states of TiO_2 and TiS_2:

$$E_{\mathrm{f}}^{\mathrm{TiOS}} = \big(E((\mathrm{TiOS})_n) - (n/2n_1 \times E((\mathrm{TiS_2})_{n_1}) + n/2n_2 \times E((\mathrm{TiO_2})_{n_2}))\big)/N, \quad (4)$$

where $E((\mathrm{TiS_2})_{n_1})$ and $E((\mathrm{TiO_2})_{n_2})$ are the total energies of unit cells of the most stable TiS_2 and TiO_2, respectively, n_1 and n_2 are the numbers of formulas per unit cell of TiS_2 and TiO_2, respectively. The calculation results are shown in Fig. 1(b). The formation energy of TiOS_$P2_1/m$ is approximately 0.059 eV/atom, and that of TiOS_$P3m1$ is 0.074 eV/atom. For the TiOS_$P4/nmm$ structure based on atomic transmutation of rutile TiO_2 reported in previous papers,[61] the formation energy is 0.194 eV/atom. The formation energies of both TiOS_$P2_1/m$ and TiOS_$P3m1$ are close to the 90th percentile of metastable phase existence criterion, which is 0.067 eV/atom,[62] and are much lower than the energy of TiOS_$P4/nmm$,[61] therefore proving their energy stability.

The crystal structures of the TiOS_$P2_1/m$ and TiOS_$P3m1$ are shown in Figs. 1(c) and 1(d), respectively. Both configurations use Ti atoms as bridges to connect O and S atoms and Ti atoms are located at the center point of the hexagon, surrounded by three O and three S atoms. Meanwhile, both of them are quasi-layered structures with weak interactions between layers. Differently, the unit cell of TiOS_$P2_1/m$ contains a total of 6 atoms, and the lattice parameters are $a = 6.30$ Å, $b = 3.22$ Å, $c = 5.53$ Å, and, $\alpha = 90.00°$, $\beta = 91.45°$, $\gamma = 90.00°$ with atomic positions at Ti, $2e$(0.01, 0.25, −0.27), O, $2e$(−0.14, 0.25, −0.60), S, $2e$(−0.23, −0.25, −1.08). The thickness of its monolayer is approximately 3.08 Å. The two types of Ti–O bond lengths l_1, l_2 are 2.04 Å, 1.96 Å, respectively, and the Ti–S bond lengths l_3, l_4 are 2.47 Å, 2.38 Å. The unit cell of TiOS_$P3m1$ only contains three atoms, and the lattice parameters are $a = b = 3.18$ Å, $c = 5.91$ Å, and $\alpha = \beta = 90.00°$, $\gamma = 120.00°$ with atomic positions at Ti, $1a$(0.00, 0.00, 0.04), O, $1b$(0.33, 0.67, 0.18), S, $1c$(0.67, 0.33, 0.78). The bond lengths of Ti–O and Ti–S are 1.99 Å and 2.43 Å, respectively, with the thickness of a single layer being approximately 2.38 Å.

The dynamical stabilities of both the TiOS_$P2_1/m$ and TiOS_$P3m1$ phases are confirmed by calculating the phonon dispersion spectra. As shown in Figs. 2(a) and 2(b), for both the TiOS_$P2_1/m$ and TiOS_$P3m1$, there are almost no imaginary frequency, which implies that they are dynamically stable. Figures 2(c) and 2(d) show the results of first principles molecular dynamics simulations at 300 K for TiOS_$P2_1/m$ and TiOS_$P3m1$ supercells. The total energy fluctuations gradually decrease with time, and the single layer atomic arrangements of the final stable structures are almost identical with the initial intra layer structures, only producing a small displacement between layers, which confirm the thermal stability of these two structures at room temperature.

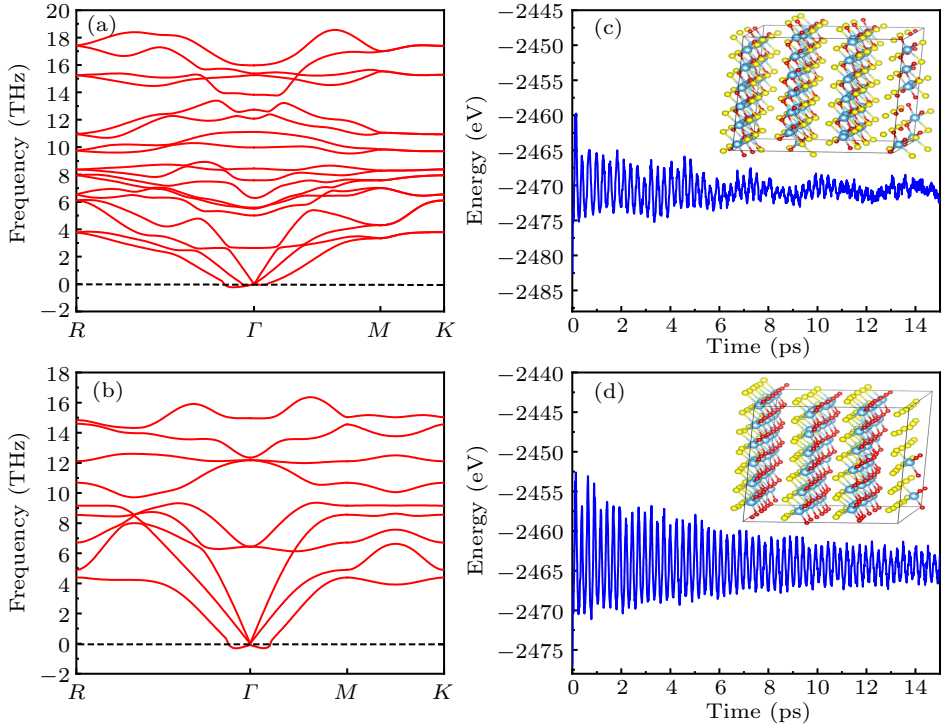


Fig. 2. The phonon spectra for TiOS_$P2_1/m$ (a) and TiOS_$P3m1$ (b). The energy profiles in AIMD simulations at 300 K for TiOS_$P2_1/m$ (c) and TiOS_$P3m1$ (d). The insets are the snapshots taken at the end of each simulation.

3.2. Electronic band structure

One of the reasons that hinder TiO_2 to be a good photocatalytic material is its wide band gap, which leads to ineffective absorption in the visible light range. However, the band gaps of the two stable TiOS structures we have newly discovered are both moderate, theoretically capable of generating sufficient electron transitions in the visible light range. As shown in Figs. 3(a) and 3(b), we use HSE06 functional to recalculate the band structures of TiOS_$P2_1/m$ and TiOS_$P3m1$. TiOS_$P2_1/m$ has an indirect band gap of 1.38 eV with VBM at Γ point and CBM along the path from A to E in the Brillouin zone. TiOS_$P3m1$ has a direct bandgap of 1.28 eV with both CBM and VBM at Γ point.

Figures 3(c) and 3(d) show the projected density of states (PDOS) on the Ti, O, S atomic orbitals for the two structures and the insets in Figs. 3(c) and 3(d) show the partial charge density of band edge states for TiOS_$P2_1/m$ and TiOS_$P3m1$, respectively. Both structures follow the conventional p–d orbital hybridization method, with CBM mainly contributed by the d-orbital of Ti atoms and VBM mainly contributed by the p-orbitals of S atoms and O atoms. It is worth mentioning that S 3p state is well hybridized in the VBM, resulting in no defect states in the band gaps.

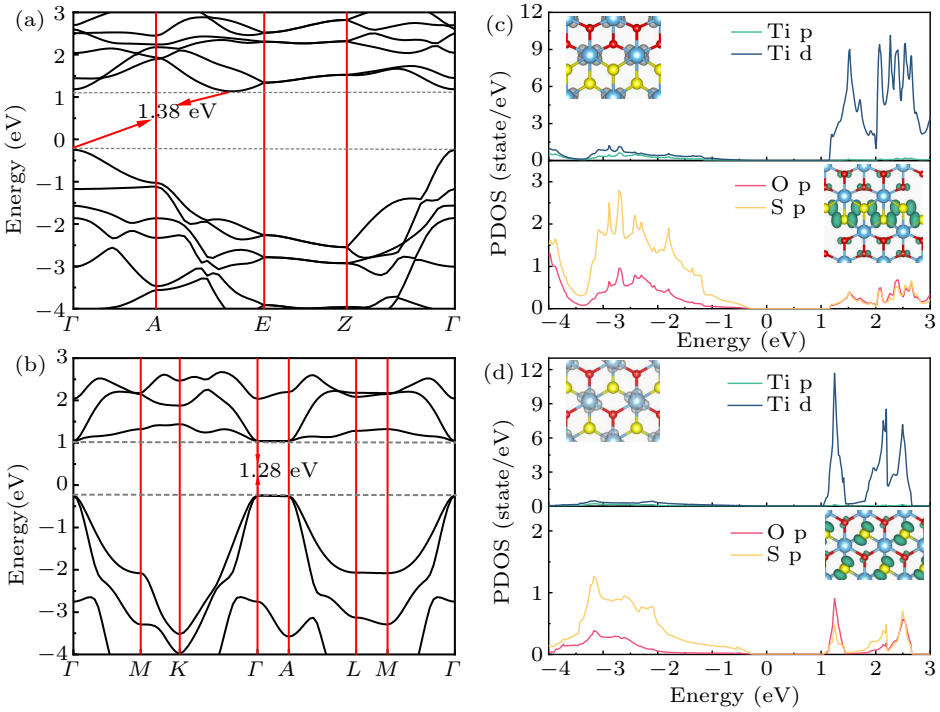


Fig. 3. Band structures for TiOS_$P2_1/m$ (a), TiOS_$P3m1$ (b), and the PDOS of (c) TiOS_$P2_1/m$, (d) TiOS_$P3m1$. Partial charge density of the VBM (green) and CBM (gray) are shown in the insets.

3.3. Photocatalytic applications

To study the photocatalytic properties, the first step is to obtain its optical absorption spectrum, ensuring that it has high optical absorption efficiency within the appropriate energy range. We use HSE06 functional to calculate the optical absorption coefficients of the materials and compare them with the absorption coefficients of three typical TiO_2 configurations: anatase, rutile, and brookite. As shown in Fig. 4(a), Obviously, compared with the typical TiO_2 configurations, TiOS_$P2_1/m$ and TiOS_$P3m1$ exhibit significant red shifts of the absorption edges, especially the TiOS_$P3m1$ whose effective optical absorption range extends to the infrared region. The absorption spectra of these two TiOS structures cover the entire visible light region, demonstrating their excellent optical absorption performance. In order to obtain more accurate optical absorption properties of TiOS_$P2_1/m$ and TiOS_$P3m1$, taking into account the exciton effect of electron–hole pairs during photoexcitation, we also use the GW–BSE and GW–RPA (G_0W_0) methods to provide quantitative optical spectra based on the imaginary parts of dielectric functions and compared them with the results using the HSE06 functional, as shown in Figs. 4(b) and 4(c). As quantified by Rubio's group using TiO_2 as an example, the inclusion of the quasiparticle description (G_0W_0) improves the electronic band gap description (the potentials for the production of H_2 or the electronic charge injection in solar cells) while GW–BSE includes the excited electron and hole interactions.[63] Therefore, we can observe that the energies of the absorption onsets obtained by the BSE method are lower, which is close to the absorption edges under the HSE06 functional. And due to the exciton effect, the spectra obtained by the BSE method have a significant absorption peak near the absorption edges. Overall, the energies of the absorption onsets under the three methods are

all less than or close to 1.6 eV, with small deviations among them, further verifying the excellent absorption and utilization efficiency of these two new materials for visible light.

As an excellent photocatalyst that can utilize visible light for water decomposition, it not only requires sufficient optical absorption within the visible light range, but also requires appropriate band alignments with water. Therefore, we also perform calculations on the positions of the CBM and VBM, using the G_0W_0 approximation method as it describes the electronic band gap better, as shown in Fig. 4(d). Generally speaking, the band edge of the material must straddle the redox potentials of water, which is related to the pH values of the water decomposition reaction. The standard[64] reduction potential of H^+/H_2 and oxidation potential of O_2/H_2O can be estimated by

$$E^{H^+/H_2} = -4.44 + \mathrm{pH} \times 0.059, \tag{5}$$

$$E^{O_2/H_2O} = -1.23 + E^{H^+/H_2}. \tag{6}$$

The TiOS_$P2_1/m$ and TiOS_$P3m1$ structures studied in this article are quasi-layered systems, so their CBM and VBM relative to vacuum level can be calculated by

$$E_{\mathrm{CBM}} - E_{\mathrm{VAC}} = \left(E^{\mathrm{GW}}_{\mathrm{CBM}} - E^{\mathrm{GW}}_{\mathrm{Fermi}}\right) + \left(E^{\mathrm{PBE}}_{\mathrm{Fermi}} - E^{\mathrm{PBE}}_{\mathrm{VAC}}\right), \tag{7}$$

$$E_{\mathrm{VBM}} - E_{\mathrm{VAC}} = E_{\mathrm{CBM}} - E_{\mathrm{VAC}} - E_{\mathrm{g}}, \tag{8}$$

where $E^{\mathrm{GW}}_{\mathrm{CBM}}$, $E^{\mathrm{GW}}_{\mathrm{Fermi}}$, and E_{g} represent the positions of CBM, the Fermi level, and the band gap obtained under the GW approximation method, respectively. $E^{\mathrm{PBE}}_{\mathrm{Fermi}}$ and $E^{\mathrm{PBE}}_{\mathrm{VAC}}$ are the Fermi level and the electrostatic potential in vacuum calculated using the PBE functional, respectively. Figure 4(d) shows the energy positions of the standard reduction potentials of H^+/H_2 and the oxidation potentials of O_2/H_2O at different pH values, as well as the relative energy level positions of CBM and VBM of the TiOS_$P2_1/m$ and TiOS_$P3m1$. It can be seen that the VBM of TiOS_$P2_1/m$ is lower than the oxidation potential of O_2/H_2O at pH = 0, and its CBM is higher than the reduction potential of H^+/H_2 at pH = 7, proving that it can consistently exhibit good photocatalytic efficiency from acidic to neutral environments. The VBM of TiOS_$P3m1$ is slightly higher than the oxidation potential of O_2/H_2O at pH = 0 and lower than the oxidation potential at pH = 7, and its CBM is higher than the reduction potential of H^+/H_2 at pH = 7 but slightly lower than the reduction potential at pH = 14. Specifically, by substituting the energies of its CBM and VBM into formulas (5) and (6), we find that its CBM position is roughly aligned with the reduction potential of water at pH = 10.84, and its VBM position is roughly aligned with the oxidation potential of water at pH = 1.19. Therefore, it proves that TiOS_$P3m1$ can serve as a good water decomposition photocatalyst within the pH range of 1.19 to 10.84.

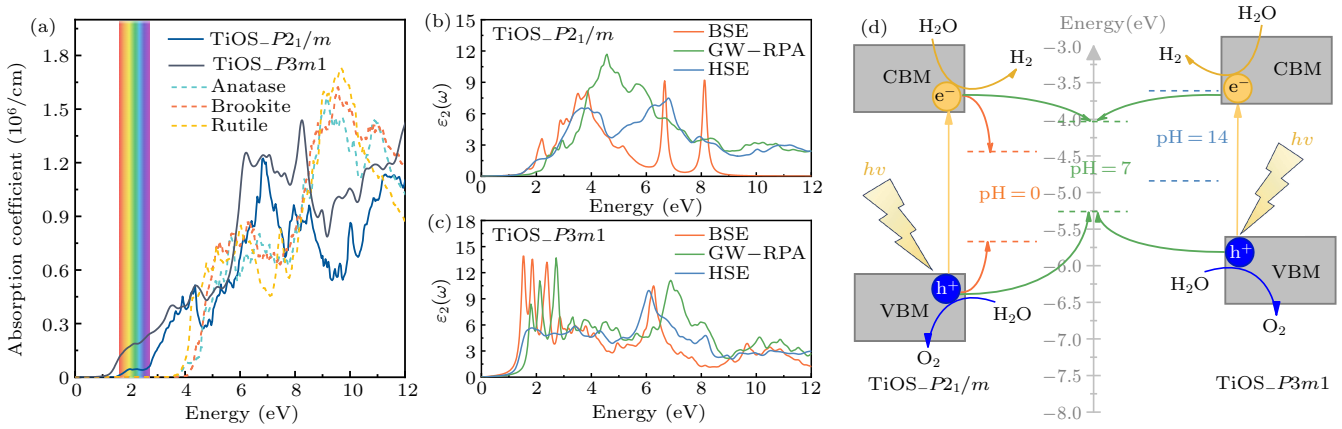


Fig. 4. Optical absorption and photocatalysis (a) optical absorption coefficients (averaged over all polarization directions) of TiOS_$P2_1/m$, TiOS_$P3m1$ and rutile, anatase, and brookite TiO_2. Imaginary parts of the dielectric functions (averaged over all polarization directions) versus incident photon energies (in eV) obtained by GW-BSE, GW-RPA, and HSE methods for TiOS_$P2_1/m$ (b), TiOS_$P3m1$ (c). (d) A schematic plot of the band alignments of the TiOS_$P2_1/m$ and TiOS_$P3m1$ relative to the water redox potentials at different pH values. The band gaps of both TiOS phases here are evaluated using the G_0W_0 level.

4. Conclusions

In summary, by applying the multi-dimensional global optimization method, we have predicted two different configurations of TiOS with desirable band gaps for photovoltaic application. The two new configurations have $P2_1/m$ and $P3m1$ symmetries, respectively, and both exhibit chemical, dynamical, and thermal stabilities. The energy bands and optical absorption spectra are calculated using the state-of-art HSE06 functional and GW approach, and the optical absorption spectra of the two new TiOS configurations predicted in this work show the significant red shifts when compared to TiO_2, demonstrating the excellent optical absorption efficiency of TiOS_$P2_1/m$ and TiOS_$P3m1$ throughout the visible light range. In addition, the energy levels of VBM and CBM with respect to the vacuum level are accurately calculated and compared with the redox potentials of water at different pH values. It is found that TiOS_$P2_1/m$ has good photocatalytic efficiency in acidic to neutral environments, while the effective photocatalytic range of TiOS_$P3m1$ is between pH = 1.19

and pH = 10.84. As demonstrated using the case of TiOS, the multi-dimensional global optimization method could lead to innovative discovery of multicomponent compounds in various functional materials design.

Acknowledgements

Project supported by the Natural Science Foundation of WIUCAS (Grant Nos. WIUCASQD2023004 and WIUCASQD2022025), the National Natural Science Foundation of China (Grant Nos. 12304006, 12104452, 12022508, 12074394, and 12374061), the Shanghai Science and Technology Innovation Action Plan (Grant No. 23JC1401400), and the Natural Science Foundation of Wenzhou (Grant No. L2023005). The computational resources are provided by the High-Performance Computing Cluster of Wenzhou Institute, UCAS and Inner Mongolia Zhongke Supercomputing Technology Co., Ltd.

References

[1] Grant F A 1959 *Rev. Mod. Phys.* **31** 646
[2] Diebold U 2003 *Surf. Sci. Rep.* **48** 53
[3] Diasanayake M A K L, Senadeera G K R, Sarangika H N M, Ekanayake P M P C, Thotawattage C A, Divarathne H K D W M N R and Kumari J M K W 2016 *Mater. Today: Proc.* **3** S40
[4] Zakir O, Ait-Karra A, Idouhli R, Khadiri M, Dikici B, Aityoub A, Abouelfida A and Outzourhit A 2023 *J. Solid State Electr.* **27** 2289
[5] Pourmadadi M, Rajabzadeh-Khosroshahi M, Eshaghi M M, Rahmani E, Motasadizadeh H, Arshad R, Rahdar A and Pandey S 2023 *J. Drug Deliv. Sci. Tec.* **82** 104370
[6] Ge S, Sang D, Zou L, Yao Y, Zhou C, Fu H, Xi H, Fan J, Meng L and Wang C 2023 *Nanomaterials* **13** 1141
[7] Ding H, Zha D, Han S and Jiang N 2023 *J. Taiwan Inst. Chem. E* **151** 105135
[8] Fujishima A and Honda K 1972 *Nature* **238** 37
[9] Geldasa F T, Kebede M A, Shura M W and Hone F G 2023 *Rsc Adv.* **13** 18404
[10] Tao X, Zhao Y, Wang S, Li C and Li R 2022 *Chem. Soc. Rev.* **51** 3561
[11] Corby S, Rao R R, Steier L and Durrant J R 2021 *Nat. Rev. Mater.* **6** 1136
[12] Eddy D R, Permana M D, Sakti L K, Sheha G A N, Solihudin, Hidayat S, Takei T, Kumada N and Rahayu I 2023 *Nanomaterials (Basel)* **13** 704
[13] Guo Q, Zhou C, Ma Z and Yang X 2019 *Adv. Mater.* **31** e1901997
[14] Mikrut P, Kobielusz M, Indyka P and Macyk W 2020 *Mater. Today Sustain.* **10** 100052
[15] Alagarasi A, Rajalakshmi P U, Shanthi K and Selvam P 2019 *Mater. Today Sustain.* **5** 100016
[16] Armaković S J, Savanović M M and Armaković S 2023 *Catalysts* **13** 26
[17] Wang J, Guo R T, Bi Z X, Chen X, Hu X and Pan W G 2022 *Nanoscale* **14** 11512
[18] Singh R and Dutta S 2018 *Fuel* **220** 607
[19] Baig U, Uddin M K and Sajid M 2020 *Mater. Today Commun.* **25** 101534
[20] Prakash J, Samriti, Kumar A, Dai H, Janegitz B C, Krishnan V, Swart H C and Sun S 2021 *Mater. Today Sustain.* **13** 100066
[21] Li Y, Shen Q Q, Guan R F, Xue J B, Liu X G, Jia H S, Xu B S and Wu Y C 2020 *J. Mater. Chem. C* **8** 1025
[22] Ji J, Liu B Y, Huang H, Wang X X, Yan L Y, Qu S J, Liu X, Jiang H R, Duan M J, Li Y F and Li M C 2021 *J. Mater. Chem. C* **9** 7057
[23] Wang J T, Fu K, Zhang X Y, Yin Q J, Wei G and Su Z Q 2021 *J. Mater. Chem. C* **9** 8466
[24] Schneider J, Matsuoka M, Takeuchi M, Zhang J, Horiuchi Y, Anpo M and Bahnemann D W 2014 *Chem. Rev.* **114** 9919
[25] Xing M, Fang W, Nasir M, Ma Y, Zhang J and Anpo M 2013 *J. Catal.* **297** 236
[26] Zhang J, Wu Y, Xing M, Leghari S A K and Sajjad S 2010 *Energ. Environ. Sci.* **3** 715
[27] Etghani S A, Ansari E and Mohajerzadeh S 2019 *Sci. Rep-Uk.* **9** 17943
[28] Zhong J, Chen F and Zhang J 2010 *J. Phys. Chem. C* **114** 933
[29] Piątkowska A, Janus M, Szymański K and Mozia S 2021 *Catalysts* **11** 144
[30] Umezawa N, Janotti A, Rinke P, Chikyow T and Van de Walle C G 2008 *Appl. Phys. Lett.* **92** 041104
[31] Umebayashi T, Yamaki T, Itoh H and Asai K 2002 *Appl. Phys. Lett.* **81** 454
[32] Huang Z, Gao Z, Gao S, Wang Q, Wang Z, Huang B and Dai Y 2017 *Chin. J. Catal.* **38** 821
[33] Sharotri N and Sud D 2015 *New J. Chem.* **39** 2217
[34] Bu X, Wang Y, Li J and Zhang C 2015 *J. Alloys Compd.* **628** 20
[35] Lin Y H, Chou S H and Chu H 2014 *J. Nanopart. Res.* **16** 2539
[36] Kovacic M, Perovic K, Papac J, Tomic A, Matoh L, Zener B, Brodar T, Capan I, Surca A K, Kusic H, Stangar U L and Loncaric Bozic A 2020 *Materials (Basel)* **13** 1621
[37] Ramanathan R and Bansal V 2015 *Rsc Adv.* **5** 1424
[38] El Nemr A, Helmy E T, Gomaa E A, Eldafrawy S and Mousa M 2019 *J. Environ. Chem. Eng.* **7** 103385
[39] Shvadchina Y O, Cherepivskaya M K, Vakulenko V F, Sova A N, Stolyarova I V and Prikhodko R V 2016 *J. Water Chem. Techno+.* **37** 283
[40] Zhang Q, Wang J, Yin S, Sato T and Saito F 2008 *J. Am. Ceram. Soc.* **87** 1161
[41] Cui Y, Du H and Wen L 2009 *Solid State Commun.* **149** 634
[42] Harb M, Sautet P and Raybaud P 2013 *J. Phys. Chem. C* **117** 8892
[43] Chen Q, Liu M, He K and Li B 2014 *Int. J. Photoenergy* **2014** 816234
[44] Jovanović D, Zagorac D, Matović B, Zarubica A and Zagorac J 2021 *Acta Crystallographica Section B Structural Science, Acta Crystallogr. B* **77** 833
[45] Schleife A, Rinke P, Bechstedt F and Van de Walle C G 2013 *J. Phys. Chem. C* **117** 4189
[46] Basera P, Saini S and Bhattacharya S 2019 *J. Phys. Chem. C* **7** 14284
[47] Thatribud A 2019 *Mater. Res. Express* **6** 095021
[48] Zhang Y Y, Gao W, Chen S, Xiang H and Gong X G 2015 *Comp. Mater. Sci.* **98** 51
[49] Chen H Z, Zhang Y Y, Gong X and Xiang H 2014 *J. Phys. Chem. C* **118** 2333
[50] Blochl P E 1994 *Phys. Rev. B* **50** 17953
[51] Kresse G and Hafner J 1994 *Phys. Rev. B* **49** 14251
[52] Kresse G and Furthmuller J 1996 *Comp. Mater. Sci.* **6** 15
[53] Kresse G and Furthmuller J 1996 *Phys. Rev. B* **54** 11169
[54] Kresse G and Joubert D 1999 *Phys. Rev. B* **59** 1758
[55] Perdew J P, Burke K and Ernzerhof M 1996 *Phys. Rev. Lett.* **78** 1396
[56] Monkhorst H J and Pack J D 1976 *Phys. Rev. B* **13** 5188
[57] Heyd J, Scuseria G E and Ernzerhof M 2003 *J. Chem. Phys.* **118** 8207
[58] Togo A and Tanaka I 2015 *Scripta Mater.* **108** 1
[59] Hybertsen M S and Louie S G 1986 *Phys. Rev. B* **34** 5390
[60] Onida G, Reining L and Rubio A 2002 *Rev. Mod. Phys.* **74** 601
[61] Barhoumi M, Said I, Yedukondalu N and Said M 2023 *Results Phys.* **48** 106438
[62] Sun W, Dacek S T, Ong S P, Hautier G, Jain A, Richards W D, Gamst A C, Persson K A and Ceder G 2016 *Sci. Adv.* **2** e1600225
[63] Chiodo L, García-Lastra J M, Iacomino A, Ossicini S, Zhao J, Petek H and Rubio A 2010 *Phys. Rev. B* **82** 045207
[64] Chen S and Wang L W 2012 *Chem. Mater.* **24** 3659